electronics

MDPI

Article

Magnetic Resonance Wire Coil Losses Estimation with Finite-Difference Time-Domain Method

Giulio Giovannetti [1,*], Yong Wang [2], Naveen Kumar Tumkur Jayakumar [2], Jeff Barney [2] and Gianluigi Tiberi [3]

[1] Institute of Clinical Physiology, National Research Council, 56124 Pisa, Italy
[2] Remcom Inc., 315 S Allen St Suite 416, State College, PA 16801, USA; yong.wang@remcom.com (Y.W.); naveen.tj@remcom.com (N.K.T.J.); jeff.barney@remcom.com (J.B.)
[3] School of Engineering, London South Bank University, 103 Borough Road, London SE1 0AA, UK; tiberig@lsbu.ac.uk
* Correspondence: giovannetti@ifc.cnr.it

Abstract: Radiofrequency (RF) coils are used to transmit and receive signals in magnetic resonance (MR) systems. Optimized RF coil design has to take into account strategies to maximize the coil performance by choosing coil sizes and geometry for achieving the best signal-to-noise ratio (SNR). In particular, coil conductor and radiative loss contributions strongly affect the SNR value, with the first mainly playing a role in low-field MR systems especially, while the second could be the dominant coil loss mechanism for high-frequency tuned coils. This paper investigates the accuracy of the finite-difference time-domain (FDTD) method for separately estimating coil conductor and radiative loss contributions. Comparison with finite element method (FEM) analysis and workbench measurements performed on a home-built coil prototype permitted us to validate the simulation results. Moreover, this research, jointly with literature data on sample-induced losses estimation, demonstrates that an FDTD-based solver permits providing an SNR model for coils with various and complicated geometries.

Keywords: RF coil simulation; RF coil losses; radiation resistance; FDTD; magnetic resonance

Citation: Giovannetti, G.; Wang, Y.; Jayakumar, N.K.T.; Barney, J.; Tiberi, G. Magnetic Resonance Wire Coil Losses Estimation with Finite-Difference Time-Domain Method. *Electronics* **2022**, *11*, 1872. https://doi.org/10.3390/electronics11121872

Academic Editor: Xiaojun Chen

Received: 8 April 2022
Accepted: 13 June 2022
Published: 14 June 2022

1. Introduction

Magnetic resonance imaging (MRI) is a non-ionizing and non-invasive diagnostic technique based on the nuclear magnetic resonance (NMR) phenomenon.

In MRI systems, the radiofrequency (RF) field is generated and picked up by using coils, which should be able to support the wide field of view (FOV) with high magnetic field homogeneity in transmission and to achieve a high signal-to-noise ratio (SNR) in reception [1]. The SNR, which depends on the hardware, on the acquisition of sequence parameters and on the tissue relaxation properties, is an accepted standard for quality measurements in MR [2]. In order to design RF coils with optimized performance for a given application, an accurate simulation process is a necessary constraint. Such simulation has to permit the selection of coil parameters (sizes and conductor geometry) for ensuring the optimal SNR, which depends on the total losses (coil resistance and sample-induced resistance) [3]. The sample-induced losses are caused by RF currents in the sample, induced by the fluctuating magnetic field, and by electric fields in the sample, mainly generated by the coil capacitors, while the coil losses comprise conductor resistance and radiation resistance, which take into account cross-sectional conductor geometry and the so-called "antenna effect", respectively. Losses in the conductor can become the dominant losses contribution, especially for low-field MR systems, while radiative losses increase with the radiation frequency and coil size [4]. As described in the literature [5], sample-induced resistance can be estimated with numerical tools employing the finite-difference time-domain (FDTD) algorithm, while for coil losses, estimation, analytical formulations [6] and

finite element method (FEM) [7] were employed. In particular, the FEM provides the great advantage of appropriately modeling structures with a small radius of curvature [8].

FDTD modeling has been used in many designs. Plasmonic non-uniform nanogratings for surface plasmon resonance (SPR) sensing and imaging were studied with FDTD to determine their optical characteristics [9], as well as the optical response of a mechanically tunable ultra-narrowband optical filter based on a one-dimensional quasi-periodic photonic crystal (QPPC), and an on-chip integrated MEMS actuator was estimated with the same method [10].

FDTD was even employed for modeling the optical properties of metal nanoparticles (MNPs) and recently a 3D-optimized FDTD (OFDTD) version was proposed for reducing computational requirements and simulation time by introducing new FDTD approximation terms based on the physical events occurring during the plasmonic oscillations in MNP [11].

Even more recently [12], a least-squares finite-difference time-domain method (LS-FDTD) was formulated in order to attenuate the high-frequency non-physical modes, superimposed to the physical solution, produced by Yee's space discretization every time that time step is larger than the Courant–Friedrichs–Lewy (CFL) limit. Such a method, which provides simple central approximations for spatial derivatives in Maxwell's equations, permitted us to obtain computer implementation simplicity and considerable processing time gains.

Further developments and applications in electromagnetic simulations will be possible thanks to recent upgrades, such as the leapfrog scheme for the unconditionally stable complying divergence implicit (CDI) finite-difference time-domain (FDTD) method, characterized by unconditional stability, complying divergence and an efficient leapfrog scheme with reduced right-hand side (RHS) flops [13].

In this paper, we propose the application of an FDTD algorithm for separately estimating conductor and radiative losses in a circular loop constituted by a wire (cylindrical rod shape) conductor from 21 to 128 MHz, corresponding to a static field from 0.5 to 3.0 T. To our knowledge, this simulation approach has not been fully theoretically and experimentally validated yet for MR coil loss contribution estimation, since copper parts are usually modeled as perfect electric conductors in FDTD simulations. The final objective of this work was to demonstrate that an FDTD-based coil SNR model is able to supply all loss contributions (coil- and sample-induced resistance values) and magnetic field pattern calculation, without approximations in sample and coil geometries.

Results provided by such FDTD simulations for conductor and radiation resistance estimations were compared with analytical, FEM and workbench results obtained with a home-built coil prototype.

2. Materials and Methods

2.1. Coil Losses Estimation with Analytical Calculations

Coils' conductor resistance can be estimated with the classic formula $\boldsymbol{Rcond} = l/\sigma S$ [14], where l and S are the total conductor length and cross-sectional area, respectively, and σ is the copper conductivity ($\sigma = 5.7 \cdot 10^7$ S/m).

The calculation of such resistance for a circular loop of the $\boldsymbol{b}$ radius constituted by a wire (cylindrical-rod-shaped) conductor with radius $\boldsymbol{a}$ can be performed as:

$$\boldsymbol{R_{cond-anal}(f)} = \frac{\boldsymbol{b}}{\sigma \boldsymbol{a} \delta} \tag{1}$$

where the term δ (penetration depth) is given by [15]:

$$\delta = \sqrt{\frac{\mathbf{1}}{\sigma \pi f \mu_o}} \tag{2}$$

where $\boldsymbol{\mu_0} = 4\pi \cdot 10^{-7}$ Henry per meter (H/m) is the permeability of free space and $\boldsymbol{f}$ is the coil tuning frequency. If a hollow cylindrical conductor (pipe) is used, Equation (1) is still

valid when the conductor thickness is greater than the penetration depth; otherwise, the penetration depth term in Equation (5) has to be substituted with the conductor thickness.

The coil radiation resistance for a small loop of radius b can be calculated as [4]:

$$R_{rad-anal}=20\pi^2\left(\frac{2\pi b}{\lambda}\right)^4 \quad (3)$$

where λ is the operating wavelength and Equation (3) is valid when the loop can be classified as small ($2\pi b << \lambda$). Application of Equation (3) for practical MRI loop coils permits us to evaluate radiation resistance contribution; for example, a 2.5 cm-radius loop tuned at 207 MHz provided a radiation resistance of 27 mΩ, which is not negligible with respect to coil resistance (66 mΩ) and is relevant to SNR [16], while losses estimated at 297.2 MHz for a 3 cm-radius coil even provided a radiation resistance value of 240 mΩ when calculated with Equation (3), and a coil resistance of 105 mΩ was estimated as described in [17].

2.2. Coil Losses Estimation with FDTD Method

2.2.1. FDTD Simulation Optimization

All simulations were performed using a commercially available software XFdtd (Remcom, State College, PA, USA).

The simulated coils were constituted by a copper conductor, and to minimize the computational load and the simulation time while achieving a good degree of accuracy, an automatic non-uniform mesh (finer in the coil area) was employed.

A Gaussian broadband pulse excitation was used to simulate the coil at multiple frequencies, and perfect matched layer (PML) was employed for truncating outward waves and simulating computational domain infinite radiation boundary conditions. Curved conductor surfaces were accurately modeled with a tool employing geometric information for providing a computational domain subcellular discretization, in order to increase the simulation accuracy for a given grid resolution and, in turn, to reduce the overall simulation time and memory constraints for a given level of desired accuracy. Moreover, a correction to the material conductivity was set in order to account for the penetration depth and loss in copper for all frequencies, useful for the cases where the cell sizes are greater than the skin depth. All the simulations were performed with an automatic detection of convergence, which was set to −90 dB, that ensured complete energy decay, so that the signal even at the lowest frequencies died down sufficiently. Finally, perfect electric conductor (PEC) sheets were placed to model the losses on the surface of each cross-sectional area of coil gaps.

2.2.2. Non-Segmented Coil

The first evaluation of FDTD capability in coil losses prediction was the simulation of a 7.5 cm-radius circular coil constituted by a 0.1 cm-radius copper wire. The loop was fed with a 1A current single port, as shown in Figure 1a, and the minimum edge length was set to 0.3 × 0.28 × 0.33 mm with a time step of 0.4104 ps.

The resistance calculations were performed at the frequencies of 21.3, 42.6, 63.9, 85.2 and 127.8 MHz, corresponding to the static magnetic field from 0.5 to 3.0 T.

After estimating the radiated P_{rad} and dissipated P_{cond} powers in the system, the equivalent conductor resistances $R_{rad\text{-}FDTD}$ and $R_{cond\text{-}FDTD}$ were calculated using:

$$R_{rad-FDTD}=\frac{2P_{rad}}{I^2} \quad (4)$$

and

$$R_{cond-FDTD}=\frac{2P_{cond}}{I^2} \quad (5)$$

where I is the current in the coil.

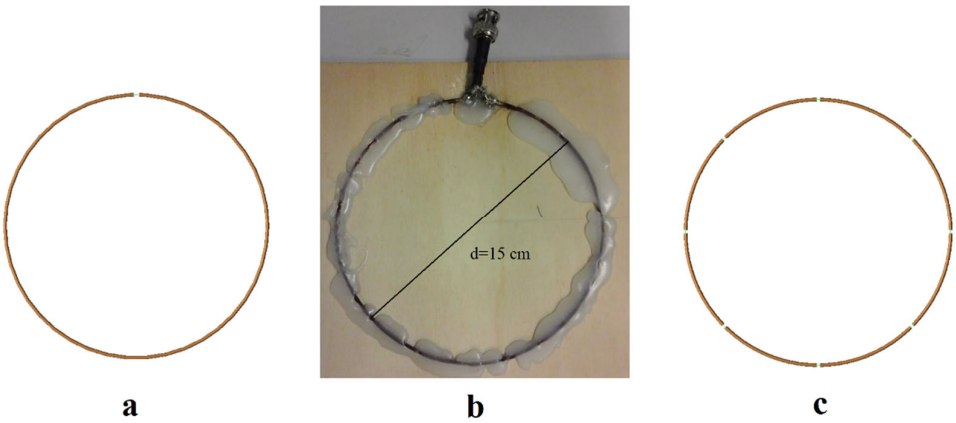

Figure 1. The investigation coil under investigation: (**a**) non-segmented simulated loop; (**b**) non-segmented home-built prototype loop; (**c**) n = 8-segment simulated loop.

2.2.3. The Tested Coil

One-feed coil simulation results were compared with those provided by a coil prototype (7.5 cm-radius loop, constituted by a 0.1 cm-radius wire, see Figure 1b) built for workbench measurements [18]. Total losses of such a coil were experimentally measured at 63.9 and 127.8 MHz with a workbench instrumentation consisting of an E5071C ENA Series Network Analyzer (Agilent Technologies, Santa Clara, CA, USA) and by connecting the coil to the analyzer with an RG58 coaxial cable and BNC connector after performing a proper calibration with the short, open, load and thru (SOLT) standard. The analyzer was set in averaging mode (64 averages) for improving measurements' sensitivity and performed with a resolution of 10 mΩ.

2.2.4. Segmented Coil

Further simulations were performed on a more realistic circular coil. In fact, to prevent that coil from starting to act as a bent dipole and the current distribution from becoming no longer uniform along the coil conductor, this second coil was segmented with 8 ports which were fed concurrently with a 1A current (Figure 1c). In this way, each coil segment was a small fraction (<1/20) of the wavelength associated with the highest simulated radiofrequency, and the same assumption made for the analytical approach of the constant current along the coil was respected. Moreover, conductor segmentation is a process which should be performed when building MR coils for reducing dielectric coupling to the coil load through conservative electric fields [4].

The simulations were performed by using concurrent feeding of the ports in the segmenting coil since it is a useful simplification of the realistic case for tuned MR coils built by inserting tuning capacitors in the gaps and feeding it only via one port. The use of these simultaneous in-phase excitations of all current sources with the same amplitudes mimics the ideal loop current distribution performing the function of the capacitors with the great advantage of the computational time reduction [19,20].

Finally, further simulations were performed by segmenting the loop with n = 2 and n = 4 brakes.

The minimum edge length was set to 0.33 × 0.33 × 0.33 mm with a time step of 0.4493 ps.

3. Results

Tables 1 and 2 show, respectively, conductor resistance and radiation resistance results for the non-segmented loop (one-feed coil) obtained by FDTD simulations at different frequencies compared with the FEM (CST—computer simulation technology, AG, Darmstadt, Germany) values [7].

Table 1. Coil conductor resistance estimation for different frequencies (non-segmented loop). FDTD and FEM calculation results.

Frequency (MHz)	$R_{cond\text{-}FDTD}$ (mΩ)	$R_{cond\text{-}FEM}$ (mΩ) [7]	Relative Difference (%)
21.3	96.26	92.25	4.35
42.6	140.69	135.65	3.72
63.9	181.07	175.37	3.25
85.2	224.56	218.97	2.55
127.8	346.46	345.11	0.39

Table 2. Coil radiation resistance estimation for different frequencies (non-segmented loop). FDTD and FEM calculation results.

Frequency (MHz)	$R_{rad\text{-}FDTD}$ (mΩ)	$R_{rad\text{-}FEM}$ (mΩ) [7]	Relative Difference (%)
21.3	0.25	0.25	0.00
42.6	4.18	4.15	0.72
63.9	22.71	21.63	4.99
85.2	79.40	85.03	6.62
127.8	549.82	574.69	4.33

By naming R_{tot} the sum of conductor resistance R_{cond} and radiation resistance R_{rad}, the experimental measurements, published previously, provided values of R_{tot} equal to 260 mΩ at 63.9 MHz and 950 mΩ at 127.8 MHz [18]. These experimental values included further resistive losses attributable to the solder joints between the coil and the cable for the connection with the analyzer (R_{sol} = 25 mΩ and 60 mΩ estimated at 64 MHz and 128 MHz [16], respectively). Total resistances R_{tot} estimated by FDTD and FEM along with experimental values reduced by soldering losses are listed in Table 3.

Table 3. Total coil resistance from experiments [18] reduced by soldering losses [16] and FEM [7] and FDTD simulations.

Frequency (MHz)	$R_{tot\text{-}measured}$ (mΩ) [16,18]	$R_{tot\text{-}FEM}$ (mΩ) [7]	$R_{tot\text{-}FDTD}$ (mΩ)
63.9	235	197	203.78
127.8	890	919.8	896.28

Tables 4 and 5 summarize, respectively, conductor resistance and radiation resistance results for the segmented loop obtained by FDTD simulations at different frequencies and compared with the analytical calculated values.

Tables 6 and 7 show, respectively, conductor resistance and radiation resistance results for the n = 2-segment loop obtained by FDTD simulations at different frequencies and compared with the analytical calculated values.

Tables 8 and 9 show, respectively, conductor resistance and radiation resistance results for the n = 4 segmented loop obtained by FDTD simulations at different frequencies and compared with the analytical calculated values.

Table 4. Coil conductor resistance estimation for different frequencies (n = 8-segment loop). FDTD and analytical calculation results.

Frequency (MHz)	$R_{cond\text{-}FDTD}$ (mΩ)	$R_{cond\text{-}anal}$ (mΩ)	Relative Difference (%)
21.3	91.56	91.21	0.38
42.6	130.15	129.00	0.89
63.9	159.35	157.99	0.86
85.2	184.47	182.43	1.12
127.8	226.99	223.43	1.59

Table 5. Coil radiation resistance estimation for different frequencies (n = 8-segment loop). FDTD and analytical calculation results.

Frequency (MHz)	$R_{rad\text{-}FDTD}$ (mΩ)	$R_{rad\text{-}anal}$ (mΩ)	Relative Difference (%)
21.3	0.25	0.25	0.00
42.6	3.95	3.97	0.50
63.9	20.01	20.09	0.40
85.2	63.30	63.50	0.31
127.8	320.72	321.48	0.24

Table 6. Coil conductor resistance estimation for different frequencies (n = 2-segment loop). FDTD and analytical calculation results.

Frequency (MHz)	$R_{cond\text{-}FDTD}$ (mΩ)	$R_{cond\text{-}anal}$ (mΩ)	Relative Difference (%)
21.3	102.40	91.21	12.27
42.6	146.77	129.00	13.78
63.9	182.42	157.99	15.47
85.2	214.64	182.43	17.65
127.8	279.76	223.43	25.21

Table 7. Coil radiation resistance estimation for different frequencies (n = 2-segment loop): FDTD and analytical calculation results.

Frequency (MHz)	$R_{rad\text{-}FDTD}$ (mΩ)	$R_{rad\text{-}anal}$ (mΩ)	Relative Difference (%)
21.3	0.25	0.25	0.00
42.6	3.99	3.97	0.60
63.9	20.54	20.09	2.25
85.2	66.07	63.50	4.04
127.8	354.03	321.48	10.13

Table 8. Coil conductor resistance estimation for different frequencies (n = 4-segment loop). FDTD and analytical calculation results.

Frequency (MHz)	$R_{cond\text{-}FDTD}$ (mΩ)	$R_{cond\text{-}anal}$ (mΩ)	Relative Difference (%)
21.3	102.54	91.21	12.42
42.6	145.94	129.00	13.13
63.9	179.37	157.99	13.53
85.2	208.32	182.43	14.19
127.8	259.87	223.43	16.31

Table 9. Coil radiation resistance estimation for different frequencies (n = 4-segment loop). FDTD and analytical calculation results.

Frequency (MHz)	$R_{rad\text{-}FDTD}$ (mΩ)	$R_{rad\text{-}anal}$ (mΩ)	Relative Difference (%)
21.3	0.25	0.25	0.00
42.6	3.96	3.97	0.17
63.9	20.14	20.09	0.24
85.2	63.94	63.50	0.70
127.8	328.26	321.48	2.11

Figure 2 depicts the plots of electric (E) and magnetic field (H) variation across the coil for the n = 2, 4 and 8 breaks at 127.8 MHz.

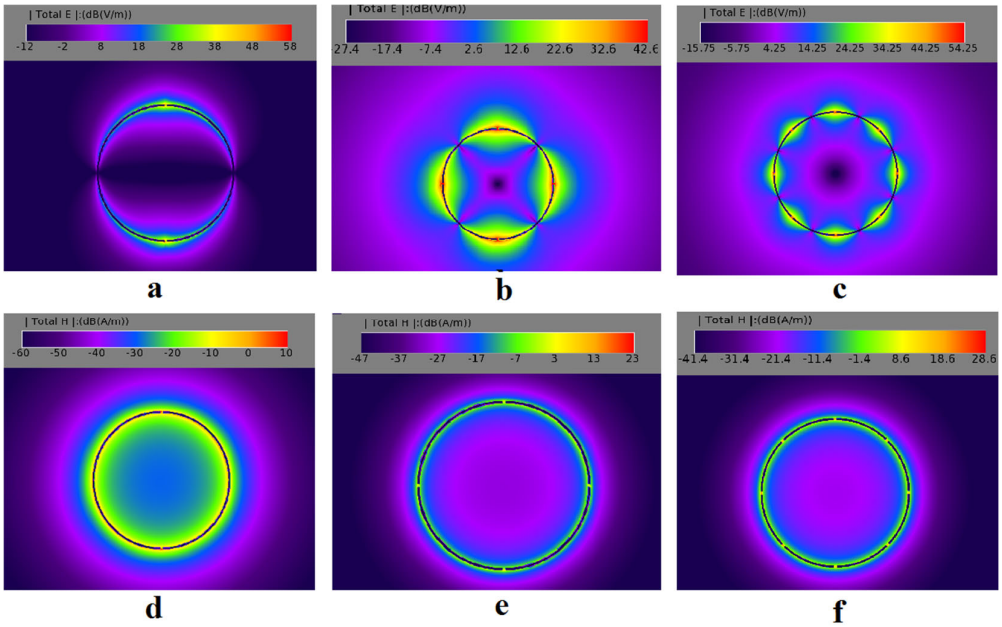

Figure 2. The field patterns for the different coil segmentation at 127.8 MHz: E field for (**a**) n = 2; (**b**) n = 4; (**c**) n = 8; H field for (**d**) n = 2; (**e**) n = 4; (**f**) n = 8.

4. Discussion

In general, FDTD-based simulation tools permit the inclusion of the computational space complex structures, such as a part of the human body, to simulate various geometry systems, without approximations in sample and coil geometries [21]. The literature described coil simulations where an SNR coil model was developed by using FDTD for

sample-induced resistance and magnetic-field pattern estimation, but the coil conductor resistance was calculated by Ohm's law, and radiation resistance was neglected [22]. However, Ohm's law can be easily applied for conductor resistance calculation only for simple coil geometries, while in some cases the radiation losses cannot be neglected, and they can be significantly different for the loaded coils and when it is placed in the scanner bore.

Although FDTD was not considered good at estimating coil losses and much inferior to FEM, we demonstrated that with an optimal simulation setup, it can provide results with a good agreement with FEM, analytical and measurement results.

In particular, for a non-segmented loop, which essentially acts as a folded dipole [23], when the loop circumference of the loop approaches a significant fraction of the wavelength, a non-uniform current flows on it. In these conditions, FDTD was able to provide results similar to the ones obtained with FEM (relative differences of <4.35% and <6.62% for, respectively, conductor and radiation resistances). Moreover, the sum of conductor resistance and radiation resistance R_{tot} calculated with FDTD provides values closer to experimental results with respect to FEM analysis, as listed in Table 3. Conversely, by segmenting this loop with $n = 8$ ports and feeding them concurrently, both conductor and radiation resistances are extremely close to the analytical method results, which contemplates a uniform current in the coil path (relative differences of <1.59% and <0.50% for, respectively, conductor and radiation resistances).

Simulation results performed with $n = 2$ and $n = 4$ breaks demonstrated that the relative difference of the FDTD-estimated coil conductor and radiation resistances with respect to analytical calculation increase when the break number diminishes, because the current distribution in the loop becomes less uniform, as can be guessed from the E field and H field patterns shown in Figure 2. In particular, for $n = 2$ the relative differences were 25.21% and 10.13% for, respectively, conductor and radiation resistances at 127.8 MHz, while the differences were reduced to 16.31% (conductor resistance) and 2.11% (radiation resistance) for $n = 4$ at the same frequency.

As predicted by theory, the radiation losses were higher in the non-segmented loop case due to the presence of larger field heterogeneities induced by the RF current phase shift on longer conductors with respect to the segmented loop. The segmentation also has the advantage of distributing the electric field all around the coil and reducing the coil antenna mode contribution [4]. We believe that the optimal number of breaks can be chosen by considering that each coil segment has to be a very small fraction (<1/20) of the wavelength associated with the highest frequency (about $\lambda/40$ in our $n = 8$ case).

5. Conclusions

Completing what is described in the literature regarding the sample-induced resistance estimation, we demonstrated that FDTD is very effective in estimating complete performance of MRI coils. In this work, FDTD results were compared with analytical and FEM ones and with workbench measurements performed on a surface RF coil prototype, demonstrating the accuracy of the FDTD method in separately estimating conductor and radiation losses in RF coils and indicating a great potential to simulate complicated coil designs that lack analytical formulas to model the losses. Future development will regard the simulation of coils in loaded conditions in order to add the estimation of the sample-induced resistance dependent on the stand-off distance between the phantom and coil and on the conductivity and permittivity of the phantom. Moreover, another future study will involve the application of the FDTD method for the simulation of RF coils constituted by rectangular cross-sectional (strip) conductors widely used in practical coil fabrication.

Author Contributions: Simulations, conception of the paper, collecting the data and drafting of the manuscript, G.G.; simulations and contribution to writing the manuscript, Y.W., N.K.T.J. and J.B.; critical revision of the article, G.T. All authors have read and agreed to the published version of the manuscript.

Funding: This research received no external funding.

Data Availability Statement: Not applicable.

Acknowledgments: The authors thank André Kuehne (MRI TOOLS GmbH, Berlin, Germany) for providing helpful comments and encouragement.

Conflicts of Interest: Yong Wang, Naveen Kumar Tumkur Jayakumar and Jeff Barney are employees of Remcom Inc.

References

1. Jin, J. *Electromagnetic Analysis and Design in Magnetic Resonance Imaging*; Routledge & CRC Press: Boca Raton, FL, USA, 1999.
2. Hoult, D.I.; Lauterbur, P.C. The sensitivity of the zeugmatographic experiment involving human samples. *J. Magn. Reson.* **1979**, *34*, 425–433. [CrossRef]
3. Giovannetti, G.; Hartwig, V.; Positano, V.; Vanello, N. Radiofrequency coils for magnetic resonance applications: Theory, design, and evaluation. *Crit. Rev. Biomed. Eng.* **2014**, *42*, 109–135. [CrossRef] [PubMed]
4. Mispelter, J.; Lupu, M.; Briguet, A. *NMR Probeheads for Biophysical and Biomedical Experiments*; Imperial College Press: London, UK, 2015.
5. Giovannetti, G.; Hartwig, V.; Landini, L.; Santarelli, M.F. Sample-Induced Resistance Estimation in Magnetic Resonance Experiments: Simulation and Comparison of Two Methods. *Appl. Magn. Reson.* **2011**, *40*, 351–361. [CrossRef]
6. Giovannetti, G. Comparison between circular and square loops for low-frequency magnetic resonance applications: Theoretical performance estimation. *Concepts Magn. Reson. Part B* **2016**, *46B*, 146–155. [CrossRef]
7. Giovannetti, G.; Tiberi, G.; Tosetti, M. Finite element method-based approach for radiofrequency magnetic resonance coil losses estimation. *Concepts Magn. Reson. Part B* **2016**, *46B*, e21348. [CrossRef]
8. Stara, R.; Fontana, N.; Tiberi, G.; Monorchio, A.; Manara, G.; Alfonsetti, M.; Galante, A.; Vitacolonna, A.; Alecci, M.; Retico, A.; et al. Validation of numerical approaches for electromagnetic characterization of magnetic resonance radiofrequency coils. *Prog. Electromagn. Res. M* **2013**, *29*, 121–136. [CrossRef]
9. Agrawal, A.K.; Ninawe, A.; Dhawan, A. Non-Uniform Narrow Groove Plasmonic Nano-Gratings for SPR Sensing and Imaging. *IEEE Access* **2021**, *9*, 10136–10152. [CrossRef]
10. Beiranvand, B.; Sobolev, A.S. Resonant-wavelength tuning of a fibonacci one dimensional photonic crystal filter at telecommunication wavelengths. *Optik* **2021**, *240*, 166926. [CrossRef]
11. Rafiee, M.; Chandra, S.; Ahmed, H.; McCormack, S.J. Optimized 3D Finite-Difference-Time-Domain Algorithm to Model the Plasmonic Properties of Metal Nanoparticles with Near-Unity Accuracy. *Chemosensors* **2021**, *9*, 114. [CrossRef]
12. de Oliveira, R.M.S.; Paiva, R.R. Least Squares Finite-Difference Time-Domain. *IEEE Trans. Antennas Propag.* **2021**, *69*, 6111–6115. [CrossRef]
13. Tan, E.L. A Leapfrog Scheme for Complying-Divergence Implicit Finite-Difference Time-Domain Method. *IEEE Antennas Wirel. Propag. Lett.* **2021**, *20*, 853–857. [CrossRef]
14. Hurlston, S.E.; Cofer, G.P.; Johnson, G.A. Optimized radiofrequency coils for increased signal-to-noise ratio in magnetic resonance microscopy. *Int. J. Imag. Syst. Technol.* **1997**, *8*, 277–284. [CrossRef]
15. Chen, C.N.; Hoult, D.I. *Biomedical Magnetic Resonance Technology*; Adam Hilger: Bristol, UK, 1989.
16. Kumar, A.; Edelstein, W.A.; Bottomley, P.A. Noise figure limits for circular loop MR coils. *Magn. Reson. Med.* **2009**, *61*, 1201–1209. [CrossRef] [PubMed]
17. Frass-Kriegl, R.; Hosseinnezhadian, S.; Poirier-Quinot, M.; Laistler, E.; Ginefri, J.-C. Multi-Loop Radio Frequency Coil Elements for Magnetic Resonance Imaging: Theory, Simulation, and Experimental Investigation. *Front. Phys.* **2019**, *7*, 237. [CrossRef]
18. Giovannetti, G.; Fontana, N.; Monorchio, A.; Tosetti, M.; Tiberi, G. Estimation of losses in strip and circular wire conductors of radiofrequency planar surface coil by using the finite element method. *Concepts Magn. Reson. Part B* **2018**, *47B*, e21358. [CrossRef]
19. Liu, W.; Collins, C.M.; Smith, M.B. Calculations of B1 distribution, specific energy absorption rate, and intrinsic signal-to-noise ratio for a body-size birdcage coil loaded with different human subjects at 64 and 128 MHz. *Appl. Magn. Reson.* **2005**, *29*, 5–18. [CrossRef] [PubMed]
20. Collins, C.M.; Smith, M.B. Spatial resolution of numerical models of man and calculated specific absorption rate using the FDTD method: A study at 64 MHz in a magnetic resonance imaging coil. *J. Magn. Reson. Imaging* **2003**, *18*, 383–388. [CrossRef]
21. Hartwig, V.; Giovannetti, G.; Vanello, N.; Landini, L.; Santarelli, M.F. Numerical Calculation of Peak-to-Average Specific Absorption Rate on Different Human Thorax Models for Magnetic Resonance Safety Considerations. *Appl. Magn. Reson.* **2010**, *38*, 337–348. [CrossRef]
22. Giovannetti, G.; Frijia, F.; Menichetti, L.; Milanesi, M.; Ardenkjaer-Larsen, J.H.; De Marchi, D.; Hartwig, V.; Positano, V.; Landini, L.; Lombardi, M.; et al. Hyperpolarized C13 MRS surface coil: Design and signal-to-noise ratio estimation. *Med Phys.* **2010**, *37*, 5361–5369. [CrossRef]
23. Hernandez, D.; Kim, K.-N. A Review on the RF Coil Designs and Trends for Ultra High Field Magnetic Resonance Imaging. *Investig. Magn. Reson. Imaging* **2020**, *24*, 95–122. [CrossRef]